
Exploration of the Effects of Confinement on the Structure and Binding Energy of Protein Complexes with Molecular Dynamics

David Laur

The University of Western Ontario

March 31, 2020

COMPLETED IN PARTIAL FULFILMENT OF 4491 COURSE
REQUIREMENTS

Supervisor: Dr. Styliani Conostas, Department of Chemistry, Western University

Table of Contents

Abstract	iii
Acknowledgments	iv
List of Abbreviations	v
List of Figures	vi
List of Tables	vii
1. Introduction	1
2. Computational Methodology	5
2.1 Molecular Mechanics Force Field	5
2.2 Basics of Molecular Dynamics	7
2.3 Simulation Set up	8
2.4 Computation of Properties	10
2.4.1 Trajectory Analysis	10
2.4.2 Hydrogen Bond Frequency	11
2.4.3 Radial Distribution Function	11
3. Results and Analysis	13
3.1 Analysis of Atomic Site Trajectories	13
3.2 Hydrogen Bond Frequency	15
3.3 Radial Distribution Function Analysis	18
3.4 Binding Free Energy Analysis	21
4. Conclusion	22
5. References	24
Appendices	A1
Appendix A Lennard-Jones Sphere C++ program	A1
Appendix B Water Box Calculations	A5
Appendix C Radial Distribution Function Script	A5
Appendix D Binding Free Energy Analysis	A6
Appendix E Hydrogen Bond Data	A9

Abstract

Nanoscale confinement has been shown to affect a variety of chemical processes. Confining environments are abundant in nature. Their effects have been observed in protein folding, ligand binding, and transition metal dimerization. However, there have not been a significant number of studies on effects of confinement on the energies and structures of water and the protein complexes. Utilizing molecular dynamics, confinement is mimicked with a spherical potential boundary (spherical cavity) containing the complex of the protease trypsin and a complementary protein inhibitor in aqueous solution. Results extracted from the binding potential energy in cavities of varying radii reflected that the maximal binding potential has an ideal cavity-to-protein volume ratio. Additionally, it was observed that within spherical cavities, proteins expand. Varying the size of the cavity and comparing it to accepted experimental values provides insight into-how the protein complex's binding is affected in the kinetically restrictive environment found throughout nature.

Acknowledgements

I would like to graciously thank Prof. Conostas who has helped me improve my research and presentation skills in a professional manner. I have learned much from her approaches to evaluating problems at their base level and I feel she has allowed me to develop a better understanding of chemistry at a fundamental level. I would also like to thank Dr. Saika-Voivod for his feedback and guidance throughout the year, Victor Kwan for his insights and suggestion into the software and programming aspects of the project and the remainder of the Conostas research group, specifically my partner Katarina Albrechtas, for their support. Finally, I would like to thank Compute Canada as well for their supply of computational resources.

Abbreviations List

BFE – Binding Free Energies

BPTI – Bovine Pancreatic Trypsin Inhibitor

Colvars – Collective Variables Module

COM – Centre of Mass

HBF – Hydrogen Bonding Frequency

MD – Molecular Dynamics

MM – Molecular Mechanics

NAMD – Nanoscale Molecular Dynamics

RDF – Radial Distribution Function

RM – Reverse Micelle

TIP3P – Three-site transferrable intermolecular potential

VDW – Van Der Waals Forces

VMD – Visual Molecular Dynamics

List of Figures

Figure 1. Kinetically restricted environments employing crowding and confinement	2
Figure 2. Depiction of attraction of hydrophobic molecules via the hydrophobic effect	3
Figure 3. Visualization of trypsin complexed with BPTI	9
Figure 4. Depiction of radial distribution functions	12
Figure 5. Root-mean-squared deviation of Trypsin/BPTI complex in a range potential boundaries with varying radii.	14
Figure 6. Histogram depicting hydrogen bond frequency within spherical confinement radii of 45 Å.	16
Figure 7. Radial distribution functions from the centre of mass of the trypsin/inhibitor complex to surrounding water in increasing radii of spherical confinement plotting probability versus radius in angstroms	18
Figure 8. Radial distribution function of water molecule oxygen atoms increasing radii of spherical confinement plotting probability density versus radial distance from reference oxygen in angstroms	20
Figure 9. Histogram depicting hydrogen bond frequency within spherical confinement radii of 50 Å.	A6
Figure 10. Histogram depicting hydrogen bond frequency within spherical confinement radii of 60 Å.	A6
Figure 11. Histogram depicting hydrogen bond frequency within spherical confinement radii of 70 Å.	A7
Figure 12. Hydrogen bond frequency versus simulation progression within spherical confinement radii of 45, 50, 60 and 70 Å	A7
Figure 13. Potential energy fluctuation versus time step within a spherical confinement radii of 45, 50, 60 and 70 Å	A9

List of Tables

Table 1. Hydrogen bond data for increasing potential boundary radii	17
Table 2. Water/water radial distribution function data for increasing radius of potential boundary	20
Table 3. Average potential energy of Colvars separated complex for increasing boundary potential radii	21
Table 4. Water box calculations to develop system of typical water density	A5

1. Introduction

From the tallest trees to the smallest cells, confinement is ubiquitous throughout nature. It can be defined as a restrictive physical boundary that hinders kinetic freedom of the enclosed system. Abiotic systems provide many examples of confinement, such as cracks developed through mechanical weathering of rocks, or atmospheric and man-made aerosols (1,2). In biotic systems, confinement is also omnipresent. An example of confinement effects in a biotic system is the capillary action of the tubular xylem of vascular plants transporting water to the leaves for photosynthesis. Cells possess examples of confinement as well. To increase efficiency, groups of cellular components are separated into confined systems in a phenomenon known as compartmentalization. The abundance of confinement in nature can be attributed to its influence on physical and chemical processes. Compartmentalization, for instance, amplifies the efficiency of biochemical processes because most reagents are found in close proximity to each other (3).

Confinement changes the chemical reactivity relative to bulk solutions. It is common to implement the confinement through the use of solvent droplets or reverse micelles (RM). RM possess hydrophobic sites outside of the micelle and a hydrophilic domain within, containing a polar solvent. An example of the dramatic effect of confinement is presented by T. Borunda et al. (4) which found that in confining RM environments, the complex $[\text{Fe}(\text{CN})_5\text{pyz}]^{3-}$ shows increased stability in dimeric form relative to monomeric counterparts. This preference contrasts the propensity in bulk solutions where the chemical equilibrium is shifted towards monomers, potentially because of the entropic effect (4). In protein systems with restrictions similar to cellular confinement, decreased rates in the diffusion of small proteins were observed due to the combined effects of the confinement and cellular crowding (5).

The effects of kinetically restricted systems on proteins is a growing field of research. A method other than confinement that restricts the system's kinetic freedom is crowding, which often

involves the use of macromolecules to hinder protein movement. Crowding has been shown to have a wide array of effects on proteins. A schematic figure of confinement and crowding around a protein are shown in Fig. 1(a) and Fig. 1(b), respectively.

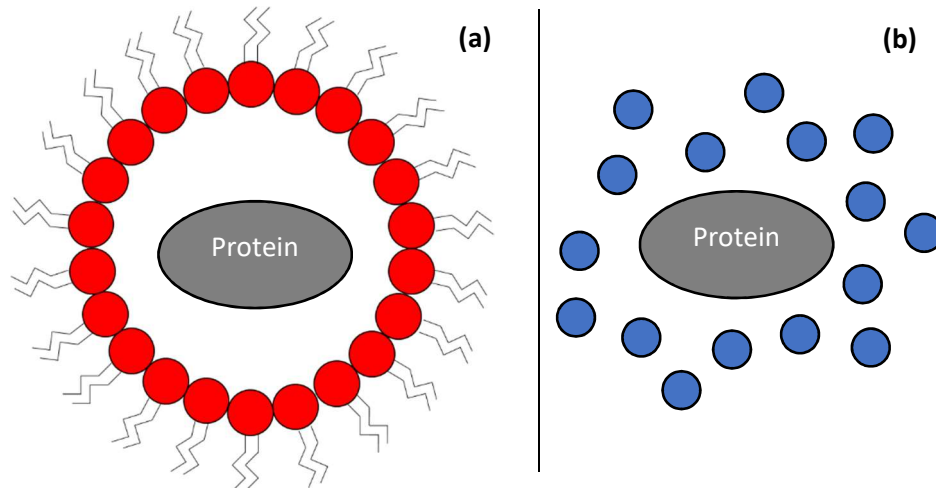


Figure 1. Kinetically restricted environments (a) Protein confined within reverse micelle confinement. (b) Protein surrounded macromolecule crowders (blue)

Proteins in crowded environments have been shown to have increased stability and rates of folding compared to proteins within a diluted solution (6, 7). In addition to this, however, crowded proteins tend to exhibit increased levels of aggregation, which has been connected to neurodegenerative disorders (8, 9). Confinement also appears to affect enzymatic activity such as in the protein *Escherichia coli* AspP which exhibits greater hydrolytic activity under restricted environments (10). There has been a large number of studies testing the effects of crowded protein systems but fewer on the behaviour of confined proteins. Studies have been performed to fine tune protein stability with boundary shape and size (11, 12). Protein folding has been shown to be significantly affected by confinement. Protein folding has generally been shown to occur at decreased rates in confined environments due to solvent-mediated stabilization of the unfolded state giving rise to a new potential energy barrier (13). A better understanding of these systems can provide insight into many factors of these protein's mechanisms within a living cell that remain

unelucidated. This includes the issue of protein's surprisingly high folding rates as explained in Levinthal's Paradox (14).

In this thesis, the effects of confinement on the free energy of binding of protein complexes are investigated. Because of time limitations, the binding free energy (BFE) was computed by averaging the potential energy of binding. This is only a part of the free energy, which requires thermodynamic integration techniques in its computation. The BFE of protein complexes is the energy associated with the non-covalent combination of two proteins through intermolecular forces. Even though a single interaction is weak, the collection of interactions is enough to start a cascade of changes in the protein structure to make the complex act as a cohesive unit. These interactions include hydrogen bonding, between hydrogen and a more electronegative atom such as oxygen or nitrogen on side chains, ionic bonds between charged polar groups near the protein surface, and van der Waals (VDW) effects, and the hydrophobic effect which draws non-polar regions to each other and has been shown to play a role in the association of protein complex subunits (15, 16). A schematic of the binding of hydrophobic sites is shown in Fig. 2, which depicts the rearrangements in the hydrogen-bonded network. The BFE will reflect the stability of the complex and can be compared to literature values of non-confined proteins to identify if the confinement posed an effect on the system.

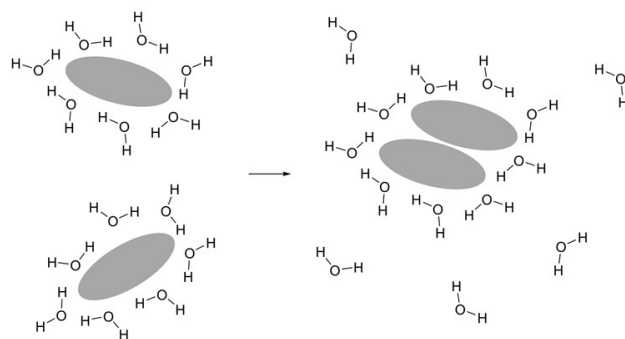


Figure 2. Depiction of attraction of hydrophobic sites in water via the hydrophobic effect. Grey ellipses represent the hydrophobic molecules.

BFE values vary greatly depending on protein composition and environment. Complexes with low BFE values are weakly bound together. They typically exhibit rapid conversion between bound and unbound protomers. This is evident from their dissociation equilibrium constant nearing one, due to the small change in free energy during complex formation. These complexes typically interact through a large quantity of transient intermolecular bonding which form and break in rapid succession. To contrast, high BFE complexes are strongly bound together and stable. This results in a very large equilibrium constant favouring protein-protein interactions over protein-solvent. Weakly bound complexes are common in signalling pathways as receptor substrates they allow for rapid response to stimuli (17). Strongly bound complexes can also be found in these pathways acting as receptors which can be activated multiple times. An example would be the insulin receptor, a stable complex made up of four subunits.

In protein molecular dynamics (MD) simulations, confinement of the system is replicated by using a spherical repulsive potential boundary. To develop an understanding of the molecular dynamics I wrote a MD code of a Lennard-Jones system of atoms which can be seen in Appendix 1.

The structure of the thesis is as follows: Section 2 will describe the methodology and background information on MD, the details for the simulations, the statistical mechanics foundation, and methods used for analysis. In Section 3, analysis and results are described for the produced simulations. The thesis closes with a conclusion and outlook.

2. Computational Methodology

2.1 Molecular Mechanics Force Field

The simulation method of MD is used to relate averages of physical properties over statistically produced molecular states with experimental observables (18). In 1957, Alder and Wainwright developed the first MD simulation using the IBM 704, the first commercial computer with the ability of floating-point binary arithmetic (19). The new technology greatly improved the complexity of calculations compared to previous models. The simulation investigated the elastic collision of hard spheres and was built on Analytical Probability Theory developed by Laplace in the early 1800s. The first realistic system was studied in 1960 by Gibson et.al which simulated radiation damage on copper (20).

The extent to which the system is recreated is dependent on the problem being posed, thus models of different levels of complexity are used, depending on the question that is investigated. Here some examples of models are presented. The study of computationally demanding systems such as large proteins or membranes often requires the use of coarse-grained models that represent groups of molecules as a single entity. Atomistic models consider each atom as an independent entity at an increased computational cost relative to coarse-grained models (21). Quantum models simulate interactions based on wavefunctions and are very computationally costly (22). With the rapid growth of high-performance computing, improved hardware advances the ability to study systems of higher complexity. To advance MD methods in terms of speed and reliability, multi-step MD integrators (21) and further contributions to the quality of charge polarization (23) are ongoing directions of research.

The potential energy of molecules in a system is often determined using molecular mechanics functions, commonly known as molecular mechanics (MM) force fields. In MM

electronic and nuclear interactions are merged together and their effect is expressed in an average way via a number of parameters, such as partial charges and atomic diameters. The potential energy between the atoms in a molecule is estimated based on the Born-Oppenheimer approximation, which states that the motion of the nuclei and electrons can be treated separately. There is a variety of force fields. Recent research attempts to create universal force fields such as the ReaxFF reactive force field (24) but they have not been generally adopted at this point in time. A general equation of MM force field is given by:

$$\begin{aligned}
 U(\mathbf{r}^N) = & \sum_{bonds} \frac{k_i}{2} (l_i - l_o)^2 + \sum_{angles} \frac{k_i}{2} (\theta_i - \theta_o)^2 + \sum_{torsions} \frac{V_n}{2} (1 + \cos(n\omega - \gamma)) \\
 & + \sum_{i+1}^N \sum_{i-j}^N \left(4\epsilon_{ij} \left[\left(\frac{\sigma_{ij}}{r_{ij}} \right)^{12} - \left(\frac{\sigma_{ij}}{r_{ij}} \right)^6 \right] + \frac{q_i q_j}{4\pi\epsilon_o r_{ij}} \right)
 \end{aligned} \quad (1)$$

The equation expresses the potential energy (U) as the sum of energetic contributions. \mathbf{r}^N denotes, in a collective manner, the positions of all the atomic sites in the system. Hereafter, in all the equations bold phase notation is used for vectors. The atomic sites are spherically shaped with diameter sigma σ . The distances are measured from the centre of an atomic site. The first three terms in the summation Eq. 1 consist of potential contributions from bonding interactions. The vibrational motion is mimicked by a harmonic spring where energy includes the parameters of the force constant k_i and the equilibrium position l_o . The harmonic bending motion of three adjacent atoms is modelled using the force constant k_i and the change in bond angle from an equilibrium angle of θ_0 . The torsional motion of groups of four non-colinear atoms having a dihedral angle is described in terms of the torsional barrier V_N and the change in torsion angle from equilibrium angle γ . The fourth term encompasses non-bonding interactions. It includes contributions from the

Lennard-Jones interactions and the Coulombic potential. The Lennard-Jones potential is expressed in terms of the potential well-depth ϵ , and σ that represents the diameter of an atomic site. It is noted that this diameter is a parameter of the force that may not represent the actual physical diameter of the atom, as measured in X-ray diffraction. The $4\epsilon \left(\frac{\sigma_{ij}}{r_{ij}}\right)^{12}$ term represents the Pauli exclusion principle (i.e. two atoms cannot overlap) and $-4\epsilon \left(\frac{\sigma_{ij}}{r_{ij}}\right)^6$ represents the attractive London dispersion forces. The coulombic potential describes the electrostatic interactions of charged atomic sites which carry partial charges. The coulombic potential is expressed in terms of the point charge parameters q , the permittivity of vacuo, which is denoted as ϵ_0 and the distance between charged sites i and j , r_{ij} .

2.2 Basics of Molecular Dynamics

Using the potential energies obtained from molecular mechanics (MM) force field equations, the resultant force can be applied to an atomic site using Newton's second law of motion:

$$\mathbf{F}_i = -\nabla U = m_i \frac{d^2 \mathbf{r}_i}{dt^2} \quad (2)$$

Where \mathbf{F}_i is the net force applied on an atomic site i from all other atoms in the system, m_i is the mass of the atom i and t denotes time. The force is expressed as the negative gradient of the potential energy ($-\nabla U$) or as a product of the mass, m , and the second derivative of the position $\frac{d^2 \mathbf{r}}{dt^2}$ which is the acceleration. With knowledge of the motion of the molecule, one can determine its trajectory. Newton's 2nd Law is a continuous second-order differential equation. This differential equation cannot be integrated analytically except for very simple forces, such as: for instance, a constant force or a quadratic force. In order to integrate Eq. (2) there are a number of

finite-difference algorithms. One algorithm frequently used is the Verlet algorithm derived originally by Jean Baptiste Delambre in 1791 (25). This algorithm is expressed as:

$$\mathbf{r}_i(t + dt) = 2\mathbf{r}_i(t) + \mathbf{r}_i(t - dt) + \left[\frac{d^2\mathbf{r}_i(t)}{dt^2}\right]dt^2$$

This algorithm expresses the atomic position vector as \mathbf{r}_i , the time is denoted by t and the time step by dt . This algorithm is time-reversible, which is in agreement with the time reversibility of Eq. (2). This is an important quality of the Verlet Algorithm because not all integration algorithms are time reversible. The Verlet Algorithm was incorporated into my MD code found in Appendix 1. The software that I used to perform the simulations uses the velocity Verlet Algorithm (26). The algorithm is expressed as:

$$\mathbf{r}_i(t + dt) = \mathbf{r}_i(t) + \mathbf{v}_i(t)dt + \frac{1}{2}\left(\frac{d^2\mathbf{r}_i(t)}{dt^2}\right)dt^2 \quad (4)$$

$$\mathbf{v}_i(t + dt) = \mathbf{v}_i(t) + \frac{1}{2}\left(\frac{d^2\mathbf{r}_i(t)}{dt^2} + \frac{d^2\mathbf{r}_i(t+dt)}{dt^2}\right)dt \quad (5)$$

This algorithm is similar to the Verlet Algorithm but expresses the atomic velocity vector as \mathbf{v}_i , atomic position vector as \mathbf{r}_i , the time is denoted by t and the time step by dt .

2.3 Simulations Set-up

The system was simulated using the software Nanoscale Molecular Dynamics (NAMD) ver. 2.13 (27) and visualized using Visual Molecular Dynamics (VMD) ver. 1.9.3 (28). The force fields utilized include the CHARMM force field package and a three-site transferrable intermolecular potential (TIP3P) water model (29, 30). The initial chemical environment consisted

of a crystal structure of the protein trypsin complexed with bovine pancreatic trypsin inhibitor (BPTI)— obtained from RCSB Protein Data Bank (PDB). The accepted literature value the BFE of the trypsin complex is 15 kcal/mol (31). Surrounding the protein, at a distance from its centre of mass (COM), a cubic water box containing 12629 water molecules, with dimensions of approximately 71 Å. (water box calculation in Appendix B) was placed. To maintain charge neutrality, 11 chloride ions were included to counteract charged sidechains. To adjust the structure of the system, the energy was minimized using conjugate gradient energy minimization, which finds atomic site positions that result in the lowest potential energy. As a result, high energy steric overlaps in the protein were eliminated. Moreover, to minimize surface energy, the water box transformed into a sphere with a radius of approximately 45 Å. A spherical boundary potential was placed around the ionized protein-water-ions drop that had a radius of 45 Å. In subsequent runs, the radius of the boundary was increased to 50 Å, 60 Å and 70 Å. In order to maintain a density of 1 g/cm³, the number of water molecules was increased to 17335, 29985, and 47650 respectively. The solvated and non-solvated representations can be seen in Fig. 3a and Fig. 3b.

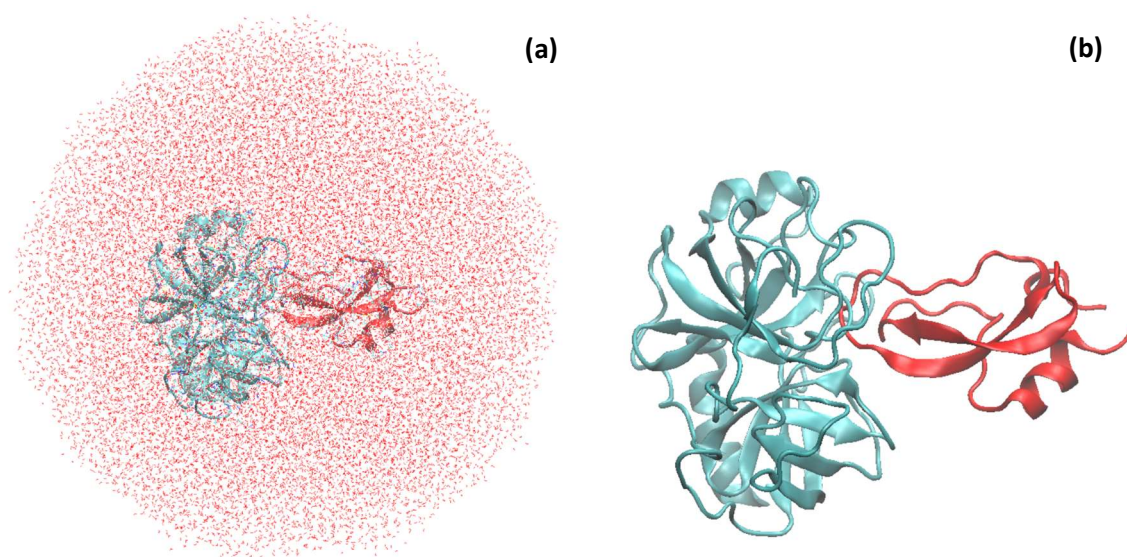


Figure 3. Typical snapshots of trypsin complexed with BPTI. (a) - solvated complex, (b) – solvated complex with water not shown for clarity

The temperature was maintained at 310 K using Langevin dynamics (32). This temperature was chosen as it reflects the typical human body temperature of 37°C. The simulation lasted one nanosecond with a timestep of 1.0 fs. Due to the stability of the complex, a very long simulation is needed for the separation of the subunits to be seen. Instead, the separation is coerced using the Collective Variables Module (Colvars) in NAMD. For each size of the repulsive boundary, the subunits are separated at two distances of 15 Å and 30 Å in separate runs.

Statistical mechanics utilizes probability and statistics to examine the properties of the systems. With statistical mechanics, macroscopic properties can be obtained from MD simulations based on the trajectories. In an MD run, the initial portion of the run is discarded as it takes time for the system to reach equilibrium.

2.4 Computation of Properties

All simulations were subjected to the analysis of atomistic trajectories, radial distribution functions (RDFs), and change in hydrogen bond frequencies (HBF).

2.4.1 Trajectory Analysis

Utilizing the software Visual Molecular Dynamics (VMD) 1.9.3, the trajectories are visualized. These trajectories provide valuable qualitative information about the behaviour of the system. This is an important step as it may indicate anomalies in the system that arise due to error, such as violation of the equipartition of energy or conservation of linear or angular momentum of the system. One example of this is the flying ice cube effect (33) in which the system moves as a cohesive unit instead of individual entities. For the confined simulations produced in this project, the overall behaviour of the trajectories were used to check for the rise of a reoccurring error in which water molecules were found outside of the potential boundary. Trajectory analysis of

specific molecules or groups of molecules can be used to explore phenomena that arise throughout the simulation.

2.4.2 Hydrogen Bond Behaviour

Intermolecular bonds between hydrogen and electronegative atoms are plentiful in the protein system. Though weak individually, the sheer number of these bonds can result in a significant force holding protein complexes together and contributing to the BFE. Fluctuations in HBF are expected but significant changes are often a result of a structural change. Some of these changes include ligand binding, protein complexation, or protein folding.

2.4.3 Radial Distribution Function

A RDF relates the probability of two systemic entities at a distance r from each other. Hence, the RDF is a spatial correlation function between two atomic sites in the radial direction (i.e. the angular orientation of the vector that points from the reference atomic site to the other one has been averaged out).

The formal expression of RDF is given as:

$$P_2 = \left[\frac{N!}{(N-2)! Z_N} \right] d\mathbf{r}_1 d\mathbf{r}_2 \int e^{\frac{-U(\mathbf{r}_N)}{k_b T}} d\mathbf{r}_1 \dots d\mathbf{r}_N \quad (6)$$

This equation solves for the probability P in terms of the number of entities N , the configuration integral Z_N , the potential energy as a function of radius $U(\mathbf{r}_N)$, Boltzmann's constant k_b and temperature T . Even though a single integral is shown in Eq. 5, the single integral represents multiple integrals over $3N-6$ coordinates. Also, the integral is finite by having limits of integration. The limits are negative infinity and positive infinity for an infinite system or between certain dimensions if the system is finite.

A schematic of RDF is shown in Fig. 4, where Fig. 4(a) shows how atoms organize around a reference atom and Fig. 4 (b) quantifies this organization using the RDF.

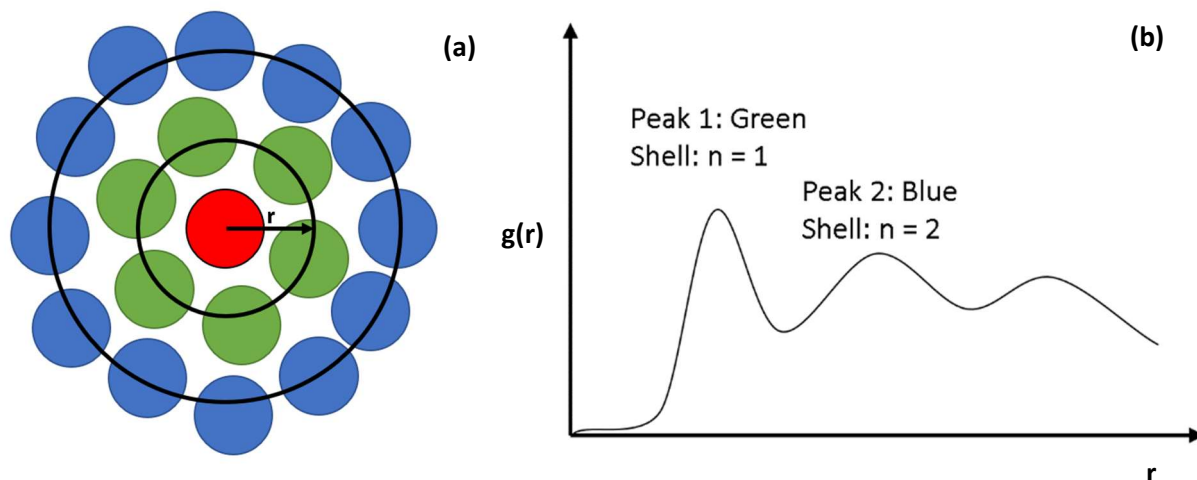


Figure 4. Depiction of radial distribution function. (a) Schematic of shell-like structures coordinating a central molecule or atom coloured red, (b) RDF (g) plot depicting the probability density of a shell as a function of radial distance from the center (red sphere).

Comparing RDF probabilities, often denoted as $g(r)$, for the variety of systems studied provides insights into how the varying certain factors is affecting the probability distribution of groups of interest. When investigating the RDF between the central atom and water, a common occurrence is the formation of water shells surround this atom. In the RDF plot, this results in peaks, the resolution of which can indicate the level of order of these shells around the reference atomic site. For the analysis of experimental data, two RDFs were developed. The first was between the protein complex COM and the oxygen site on water, the second between oxygen sites of water molecules. Both RDFs are beneficial in investigating the dynamic properties of the protein complex as well as the water.

3. Results and Analysis

3.1 Trajectory Analysis

The trajectories were obtained from simulation runs within cavities with radii of 45 Å, 50 Å, 60 Å, and 70 Å. For each cavity size, two protein configurations were examined where the protomers are separated at a distance of 15 Å and 30 Å. Trajectory analysis revealed insightful information about the behaviour of the water around the separated protein complex, nearing the cavity boundary, and penetrating towards the COM. The trajectories did not show a break-down of conservation laws or abnormalities, therefore supporting the reliability of the simulations. One abnormality includes the flying ice cube effect in which the system becomes trapped in one conformation becoming stagnant, propagating through space in a direction based on total momentum.

Separation is coerced using the Collective Variables Module (Colvars) in NAMD. For the 15 Å separation run, the complex separated over the course of 100 picoseconds. The 30 Å separation run showed the complex separating over the course of 200 picoseconds. During separation of the complex, water rapidly rushes in to fill the void between the subunits within a few picoseconds. This was observed in all simulations. Overlaying the trajectories reveals that boundary radius has minimal or no effect on this process. The water solvates the newly exposed interfaces of the complex. In real systems, solvating the interface hinders the recoordination of the complex implying it is influencing complex BFE.

In boundaries of radius 45 Å or 50 Å, the complex moved very close to the edges of the boundary. Tracking the trajectories of the water molecules that are found between the boundary and the subunit shows that as the subunit is approaching the boundary, the water undergoes a large reduction in diffusion rate, due to being confined within the protein-boundary space. This

phenomenon was only observed in potential boundaries with radii of 45 Å and 50 Å, as larger potential boundaries have sufficient space for the water to diffuse out of this space. The trajectories did not show break-down of conservation laws, therefore supporting the reliability of the simulations

By hiding the protein representation in VMD, water penetrating towards the centre of the protein could be seen. By overlaying the trajectories of the 40 Å and 70 Å boundary simulation, it was evident that there were abundantly more water molecules found in this void for the 70 Å boundary. This is indicating the protein may expand with increasing boundary radii allowing water to penetrate previously unexposed protein space. This trend can be seen when overlaying all trajectories.

This expansion was observed in the trajectories as well. Overlaying the protein complexes revealed that sidechains on the surface stretch out further in large systems. This was most prevalent in side chains with long alkyl groups, namely arginine. Since the expanded protein is the higher entropy conformation it can be concluded that in small potential boundaries, the low entropy form is preferred. This is supported by root-mean-square deviation which shows a larger distance between backbone atomic sites of the protein complex as seen in Fig. 5.

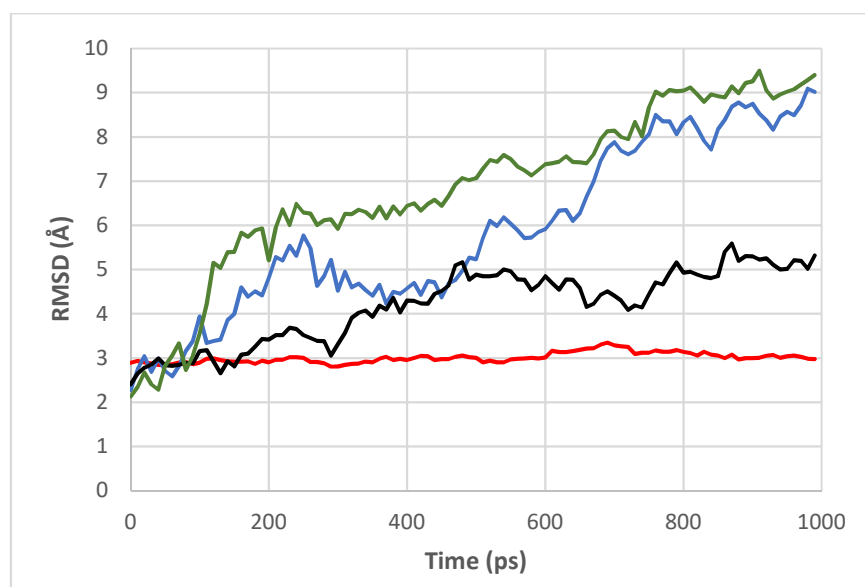


Figure 5. Root-mean-squared deviation of Trypsin/BPTI complex in a range of potential boundaries with varying radii. Red- 45 Å, Black – 50 Å, Blue – 60 Å, Green – 70 Å.

Comparing the protein complex separation, the two subunits did not completely separate during the 10 Å separation run. This was most prevalent in the more confined environments in which the complex appeared to remain more connected than in less confined counterparts. For the 20 Å separation run, all protein complexes completely dissociated.

3.2 Hydrogen Bond Analysis

All simulations experience fluctuations in HBF. There were no significant changes in the overall variations in the plots (additional plots can be found in Appendix D). Hydrogen bonds were measured with a cutoff range of 3 Å and a cutoff angle of 20°.

The general trend in the total number of hydrogen bond plots can be seen in Fig. 5. There were no significant changes in the overall variations in the plots so additional plots can be found in Appendix D. Tabulated data can be seen in Table 1.

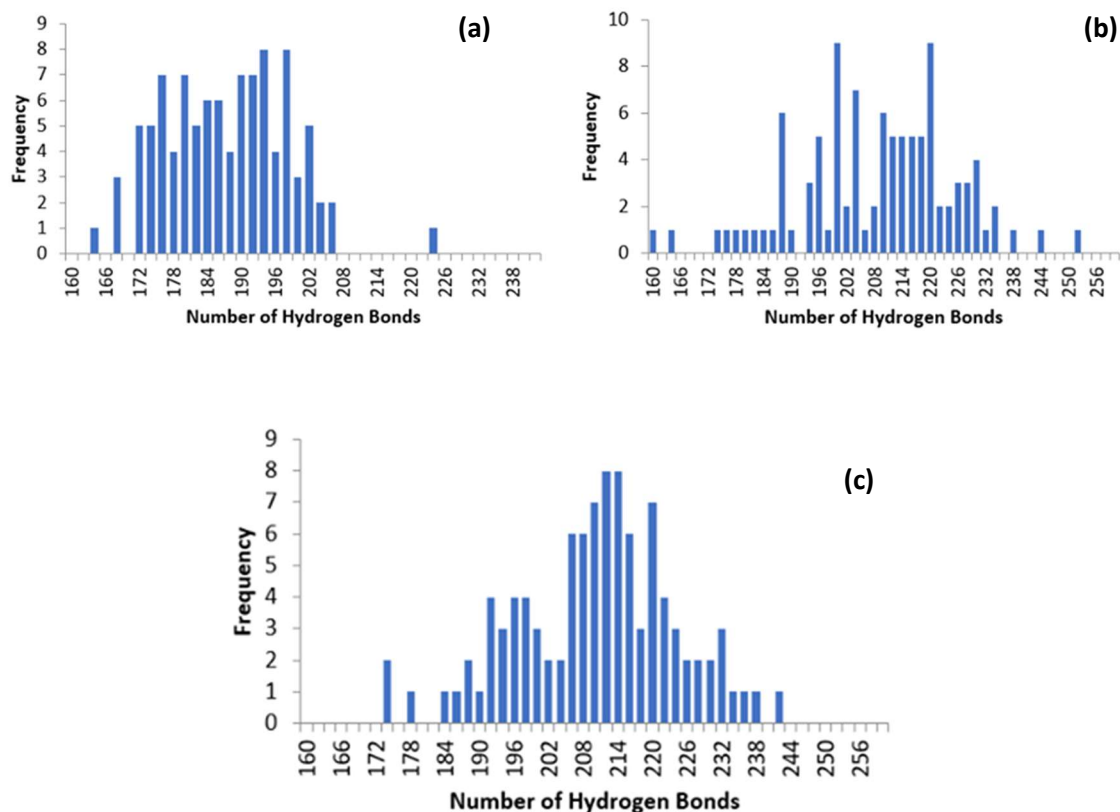


Figure 6. Histogram depicting hydrogen bond frequency within spherical confinement radii of 50 Å. (a) - 0Å, (b) - 10Å, (c) - 20 Å separation.

All systems explicated a change in HBF, data for which can be seen in Table 1. Systems separated using Colvars were shown to have a greater HBF and the mean number of hydrogen bonds. It can be rationalized that the reduce change in HBF is due to the protein complex remaining bound together. In contrast, simulations separated using the Colvars module show a significant change in the HBF. The surge in new hydrogen bonds forming can be attributed to the separation of the complex causing hydrogen bonds between the subunits to be broken. The newly exposed hydrogen bond acceptors and donors, once buried within the complex interface, readily interact with water, causing new hydrogen bonds to form. The difference between the separate and non-separated complexes are observed in the increase in mean hydrogen bonds as well. They however show no trend with increasing boundary radius.

Table 1. Hydrogen bond data as a function of cavity radius

Boundary Radius (Å)	Separation Radius (Å)	Mean Number of Hydrogen Bonds	Max Hydrogen Bonds
45	0	199.56	227
	10	211.01	253
	20	212.41	243
50	0	187.03	223
	10	208.28	252
	20	209.57	241
60	0	199.42	232
	10	203.29	238
	20	213.68	250
70	0	197.99	223
	10	207.05	237
	20	210.188	238

As the radius of the boundary increases, an increase in the rate of change of HBF is observed when comparing protein subunits separated at the same distance of either 10 or 20 Å. This supports the trajectories indicating the expansion of the protein as the boundary potential radius increases, as water is able to penetrate further into the protein to form more hydrogen bonds.

As seen in Section 3.1, proteins within a boundary potential of 45 and 50 Å get very close to the edge of this boundary, disrupting the water. Their location can explain why potential boundaries with these radii show a smaller increase in HBF for a separation of 20 Å than they do for a separation of 10 Å. As seen in the trajectories, the water between the subunit and the boundary

gets displaced, preventing a significant portion of the protein surface from hydrogen bonding. This is not seen in larger boundaries due to sufficient space for water.

3.3 Radial Distribution Function Analysis

The RDFs between the protein complex COM and surrounding oxygen sites of water were obtained, as well as RDFs between the oxygen atoms of water molecules. COM/H₂O RDFs were only produced from the trajectories of the complex protein. This is because as the protein separates the COM of the complex cannot be utilized, as it can no longer reliably describe the complex. There was a significant change in the resultant RDF as shown in Fig. 7:

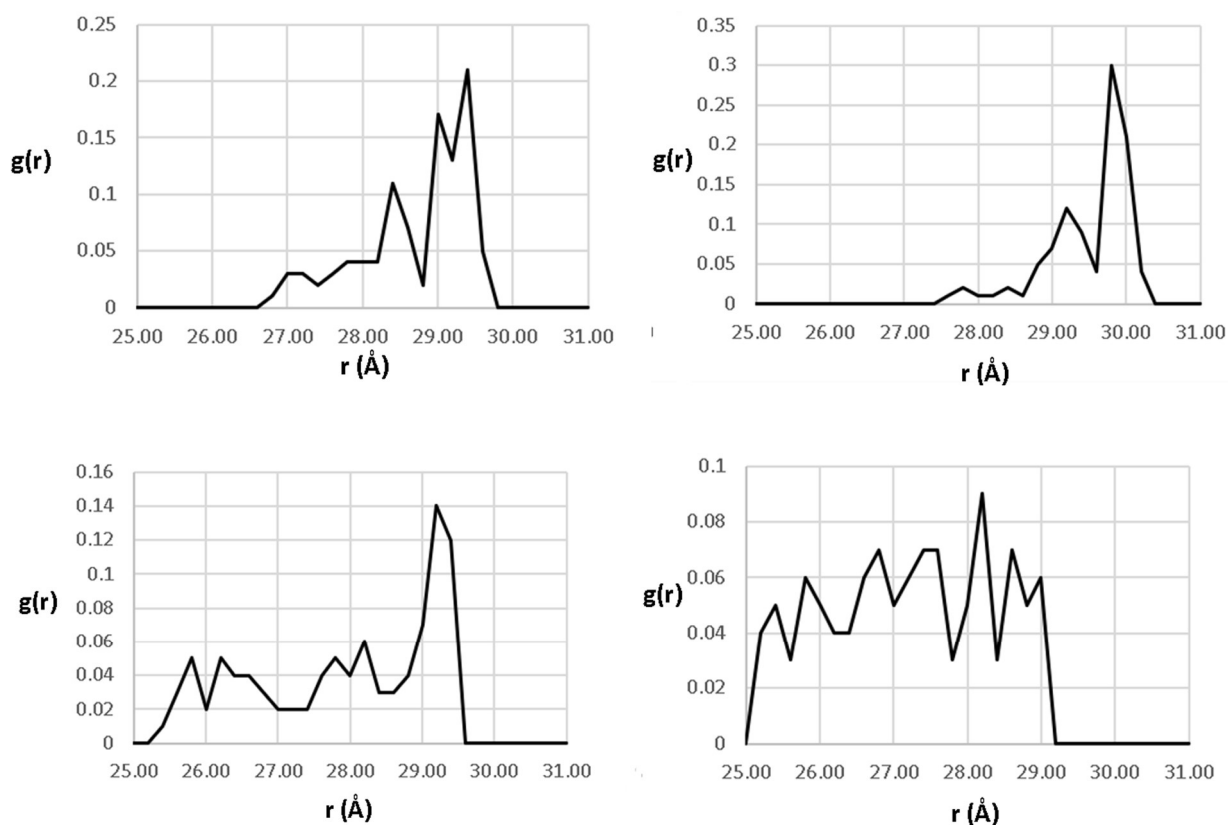


Figure 7. Radial distribution functions from the centre of mass of the trypsin/inhibitor complex to surrounding water in increasing radii of spherical confinement, plotting probability versus radius in angstroms. a) 45 Å, b) 50 Å, c) 60 Å, d) 70 Å.

As the radius of the boundary increases, the resolution of these peaks significantly decreases which is indicative of less ordered water shells surrounding the protein. Fig. 7(a) and Fig. 7(b) were similar in shape and show reasonably resolved peaks considering the spherical asymmetry of the protein complex. The distortion can be most seen in Fig. 7(d) which experiences significant depreciation in resolution, indicating a disordered solvent environment. Despite the low resolution, Fig. 7(d) does still exhibit some semblance of shell structure. The lack of order is also exhibited in peak heights. In contrast to Fig. 7(a), the 70 Å plot has peaks nearing similar heights which indicates an even distribution of the water. Finally, I would like to draw attention to the shift in these peaks towards the COM as the boundary radius increases. This may result from the protein opening up more, due to the increased kinetic freedom, which favours the higher entropy spread-out protein. The expanded protein is less dense and therefore allows water to penetrate closer to the COM. This is consistent with the penetrating trend of water discussed in Section 3.1. This can also be used to rationalize the inverse relationship of the boundary radius and peak resolution. As the protein opens it loses spherical symmetry to a greater extent making the COM less relatable to the geometric centre, therefore decreasing resolution. Physical disruption of shell formation may also occur due to outstretched charged side chains.

The trajectories of water O/O RDFs all resulted in similar plots with close overlap, as can be seen in Fig. 8:

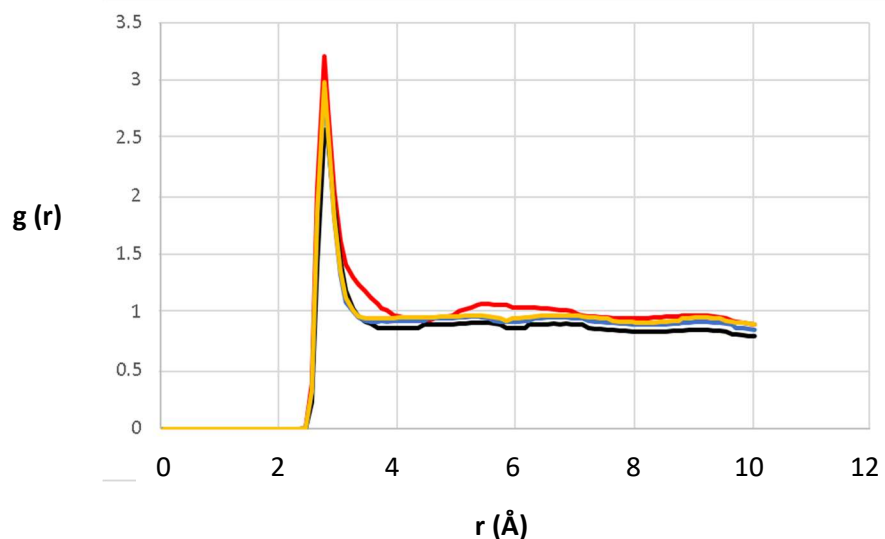


Figure 8. Radial distribution function of water molecule oxygen atoms of increasing radii of spherical confinement plotting probability density versus radial distance from reference oxygen in Å. Red - 45Å, Black - 50Å, Blue - 60 Å, Yellow - 70 Å.

There is little change in the plot shape of $g_{oo}(r)$, showing that there is little change in the water of the confined environment. The 45 Å boundary (Red) showed slightly higher peaks at first and second maxima. Following the 45 Å boundary there was a significant decline in $g_{oo}(r)$. The lower probability density of these peaks indicates an increase in distance between oxygen atoms of water. The remainder of plots data can see in Table 2.

Table 2. Oxygen/Oxygen radial distribution function data for increasing radius of potential boundary

Radius (Å)	First Maximum		Second Maximum	
	Distance (Å)	$g_{oo}(r)$	Distance (Å)	$g_{oo}(r)$
45	2.75	3.19735	5.55	1.07071
50	2.75	2.57241	5.35	0.91155
60	2.75	2.94689	5.35	0.96416
70	2.75	2.97579	5.35	0.98518

The graphs of 50, 60, and 70 Å were shown to have increasing values of $g_{oo}(r)$ with larger boundary sizes. An insufficient range of radii are studied to say for certain, but it is likely $g_{oo}(r)$

values will converge towards the literature values of $g_{oo}(r)$ in bulk water given as 3.09 and 1.14 for the first and second maxima respectively (34).

3.4 Binding Potential Energy Analysis

A very simple BFE estimation was performed using differences in potential energies of separated and complexed proteins to represent the free energy change during binding. Data for which is tabulated in Table 3.

Table 3. Average potential energy of Colvars separated complex for increasing boundary potential radii

Boundary Radius (Å)	Covars Radius (Å)	Average Potential Energy (kJ/mol)	Potential Energy Difference - BFE	
			(kcal/mol)	(kcal/mol)
45	0	-149292	0	0
	10	-149273	19	4.5400
	20	-149252	40	9.5600
50	0	-145672	0	0
	10	-145689	17	4.0631
	20	-145727	55	13.1453
60	0	-249816	0	0
	10	-249768	44	10.5163
	20	-249770	46	10.9943
70	0	-423794	0	0
	10	-423796	2	0.4780
	20	-423989	194	46.3671

As expected, complexed proteins were the more stable conformation. Similar to the transition metal complex works of T. Borunda et al. (4), the lower entropy conformation was preferred in the confined environment. This was already evident however as an extremely long

simulation would be required to see the complex separate naturally indicating the complex is the preferred conformation. In comparison to literature values of 15 kcal/mol in bulk solution (31), the protein complex generally possessed a smaller BFE when confined. This was seen in all runs except for the 70 Å cavity, which has a large BFE of 46.3671 kcal/mol. This indicates that the complex likely has an ideal ratio of protein to confinement volume, but when kinetic freedom is too restricted, BFE decreases with respect to literature bulk solution complexes. It is unclear why there is such a large change between the two separated runs of 70 Å confinement. One hypothesis is that due to the small difference between the complexed and the 10 Å separated run that the complex may still be in a favourable conformation, despite forced separation.

4. Conclusion

This thesis explored the effects of the size of spherical confining environments on the water and protein structure as well as the binding energy of the protein complex Trypsin/BPTI. Utilizing MD simulations, confined protein environments were developed with radii of cavities ranging from 45 Å to 70 Å. Using the Colvars module of NAMD, the protein complex are separated. Comparing the potential energy of the separated complex to the coordinated complex provide an approximation of the free energy of binding associated with the complex separation.

In general, the complex experiences a reduction in BFE with respect to literature values of 15 kcal/mol (31). It was found that due to the low resolution of the 70 Å system is highly disordered. Within the disorder water, the protein was found to have a very large BFE value of 46.37 kcal/mol, three times higher than in bulk water. The ordered systems of smaller confinement showed a reduction in BFE compared to literature values. This was seen most in the 45 Å system, with BFE increasing with a larger boundary radius.

The research indicates that confinement affects the structure and dynamics of the protein system. From trajectory analysis, we see clear unfavourable interactions between the protein and the walls of the confinement. For the most part, these interactions were minimized as the protein remained near the COM of the system. It is most evident in the separation runs of the 45 Å and 50 Å which displace and trap water around the edges of the boundary. The system with smaller confinement radius had a reduction in HBF as the subunits approached the boundary, indicating less of the protein surface is presently available for hydrogen bonding. This is also reflected in the potential energy data of the 45 and 50 Å simulations which experience an increase in BFE when subunits are nearing the potential boundary indicating an unfavourable interaction with boundary. A phenomenon observed was the expansion of the protein with increasing confinement radius. Overlay of trajectories showed that longer side chains near the protein surface were found further away from the complex COM, indicating an expansion. This was also observed in the trajectories of water, which penetrate further into the expanded proteins. This is supported by RDF data between the complex COM to surrounding oxygen atoms of water. Figure 6 depicts a trend of water being found closer to COM with increasing radii, indicating expansion. This was further supported by hydrogen bond data as well, which gave evidence of water penetration.

While some general information can be obtained, the simplicity of the BFE analysis method calls for a more robust free energy calculation method. The application of more accurate methods would be beneficial to explore the potential relationship of BFE and the volume ratio of protein to confinement.

5. References

1. Eppes, M.; Keanini, R. *Rev Geophys.* **2017**, 55 (2), 470-508.
2. Falkowska, M.; Bowron, DT.; Manyar, H.; Youngs TGA.; Hardacre. *CAngew.* **2018**, 57 (17), 4565-4570. xxx
3. Diekmann, Y.; Pereira-Leal, JB. *Biochem. J.* **2013**, 449 (2), 319-331.
4. Borunda, T.; Myers, AJ.; Fisher, M.; Crans, DC.; Johnson, MD. *J. Molecules.* **2018**, 23 (4), 858.
5. Watanab, C.; Yanagisawa, M. *Phys. Chem. Chem. Phys.* **2018**, 20 (13), 8842-8847.
6. Cheng, K.; Wu, Q.; Zhang, Z.; Pielak, G, Liu, M. *ChemPhysChem.* **2018**, 19, 3350-3355.
7. Betancourt, M.; Thirumalai, D. *J. Mol. Biol.* **1999**, 287 (3), 627-644.
8. Ellis, RJ.; Minton, AP. *Biol. Chem.* **2006**, 387 (5), 485-497.
9. Chaudhuri, TK.; Paul, S. *FEBS. J.* **2006**, 273 (7), 1331-1349.
10. Moran-Zorzano, MT.; Kataoka, M.; Ueoka, R. *FEBS. Lett.* **2007**, 581 (26), 1035-1040.
11. Rathore, N.; Knotts, T. *J. Biophys.* **2006**, 90 (5), 1767-1773.
12. Cheng, K.; Wu, Q.; Zhang, Z.; Pielak, G.; Liu, M.; Li, C. *ChemPhysChem.* **2018**, 19 (24), 3350-3355.
13. Lucent, D.; Vishal, V.; Pande, V. *PNAS.* **2007**, 104 (25), 10430-10434.
14. Zwanzig, R.; Szabo, A.; Bagchi, B. *PNAS.* **1992**, 89 (1), 20-22.
15. Alberts, B.; Johnson, A.; Lewis, J.; Raff, M.; Roberts, K.; Walter, P. *Molecular Biology of the Cell*, 4th ed.; Garland Science: New York., **2002**.
16. Snyder, P.; Mecinović, J.; Moustakas, D.; Thomas, S.; Harder, M.; Mack, E.; Lockett, M.; Héroux, A.; Sherman, W.; Whitesides, G. *PNAS.* **2011**, 108, 17889-17894.
17. Krowarsch, D.; Dadlez, M.; Buczek, O.; Krokoszynska, I.; Otlewski, S. *J. Mol. Biol.* **1999**, 289, 175-186.

18. Allen, MP.; Tildesley, DJ. *Computer Simulation of Liquids*, 2nd ed.; Clarendon Press: Oxford., **1987**.
19. Alder, BJ.; Wainwright, TE. *J. Chem. Phys.* **1959**, 31 (2), 431-459.
20. Gibson, JB.; Goland, AN.; Milgram, M.; Vineyard, GH. *Phys. Rev.* **1960**, 120 (4), 1229-1253.
21. Kmiecik, S. Gront, D.; Kolinski, M.; Wieteska, L.; Dawid, AE.; Kolinski, A. *Chem. Rev.* **2016**, 116 (14), 7898-7936.
22. Hofer, TS.; de Visser, S. *Front. Chem.* **2018**, 6, 357.
23. Lagardère, L.; Aviat, F.; Piquemal, J. *J. Phys. Chem. Lett.* **2019**, 10 (10), 2593-2599.
24. Lopes, P.; Guvench, O.; Mackerell, A. *Methods Mol. Biol.* **2015**, 1215, 47-71.
25. Senftle, T.; Hong, S.; Islam, M.; Kylasa, S.; Zheng, Y.; Shin, Y.K.; Junkermeier, C.; Engel-Herbert, R.; Janik, M.; Aktulga, H. et al. *NPJ Comput. Mater.* **2016**, 2 (1), 1-14.
26. Spreiter, Q.; Walter, M. J. *Comput. Phys.* 1999, 152 (1), 102-119.
27. Delambre, JB. *Histoire de l'astronomie au dix-huitième siècle.*; Paris. **2004**, 27-43.
28. Phillips, J.; Braun, R.; Wang, W.; Gumbart, J.; Tajkhorshid, E.; Villa, E.; Chipot, C.; Skeel, R.; Kalé, L.; Schulten, K. *J. Comput. Chem.* **2005**, 26 (16), 1781-1802.
29. Humphrey, W.; Dalke, A.; Schulten, K. *J. Molec. Graphics.* **1996**, 14, 33-38.
30. Karplus, M.; Brooks, B. R.; Brooks, C. L.; Mackerell, A. D.; Nilsson, L.; Petrella, R. J.; Roux, B.; Archontis, G.; Bartels, C et al. *J. Comput. Chem.* **1983**, 30 (10), 1545-1614.
31. Jorgensen, W.; Chandrasekhar, J.; Madura, JD.; Impey, RW.; Klein, M. *J. Chem. Phys.* **1983**, 79 (2), 926-935.
32. Davidchack, RL.; Ouldridge, TE. Tretyakov, MV. *J. Chem. Phys.* **2009**, 130 (14), 234101.
33. Mark, P.; Nilsson, L. *J. Phys. Chem. A.* **2001**, 105(43), 9954-9960.

6. Appendices

6.1 Appendix A – Lennard-Jones Sphere C++ Program

```
/* David Laur */
/* Brief base code for MD simulation employing verlet algorithm and
velocity rescaling, playground for MD exploration */

#include <iostream>
#include <cmath>

int N = 10; //Num of Molecules
int limit = 100; //Number of time steps
double epsilon;
double sigma; // pg. 21 CSoL
int cubelx = 6*sigma; //pg. 25 CSoL
int cubely = 6*sigma;
int cubelz = 6*sigma;
double temperature;
double pressure;
double dt = 10; //fs
bool dimensionless = true;
bool kb = 1.38E-23;

struct step
{
    double xp, yp, zp; //Next Coordinates
    double x, y, z; //Current Coordinates
    double xm, ym, zm; //Previous Coordinates
};

struct atom
{
    step pos;
    step vel;
    step force;
};
atom atom [1000];

void initialPosition()
{
    double ox, oy, oz;
    ox = 0.0; oy = 0.0; oz = 0.0;
    int n = 0;
    int i,j,k;
    for (i=0; i < cubelx; i++)
    {
        ox = i;

        for (j=0; j < cubely; j++)
        {
            oy = j;
```

```

        for (k=0; k < cubelz; k++)
        {
            oz = k;
            atom[n].pos.x = ox;
            atom[n].pos.y = oy;
            atom[n].pos.z = oz;
            n++;
        }
    }
}
for(i = 0; i <N; i++)
{
    atom[i].pos.xm = atom[i].pos.x;
    atom[i].pos.ym = atom[i].pos.y;
    atom[i].pos.zm = atom[i].pos.z;
    atom[i].vel.x = 0.0;
    atom[i].vel.y = 0.0;
    atom[i].vel.z = 0.0;
}
}

void initialForce()
{
    double rSq, fforce, dfx, dfy, dfz, fx, fy, fz, sigmaSq;
    int i,j;
    for (i=0; i < N; i++)
    {
        atom[i].force.x = 0.0;
        atom[i].force.y = 0.0;
        atom[i].force.z = 0.0;
    }
    for (i = 0; i < N - 1; i++)
    {
        for (j = 1; j < N ; j++)
        {
            dfx = (atom[i].pos.x - atom[j].pos.x);
            dfy = (atom[i].pos.y - atom[j].pos.y);
            dfz = (atom[i].pos.z - atom[j].pos.z);
            rSq = dfx*dfx + dfy*dfy + dfz*dfz;
            sigmaSq = pow(sigma,2);

            fforce = (24 * epsilon / rSq) * (2*pow(sigmaSq/rSq, 6) -
pow(sigmaSq/rSq, 3)); //rij on end of equation can be assumed as
rij^2 (pg 141 CSoL)
            fx = fforce * dfx;
            fy = fforce * dfy;
            fz = fforce * dfz;

            atom[i].force.x += fx;
            atom[i].force.y += fy;
            atom[i].force.z += fz;

            atom[j].force.x += fx;

```

```

        atom[j].force.y += fy;
        atom[j].force.z += fz;
    }
}

void T_Thermostat(double KE)
{
    int i;
    double instaT;
    double totVelSqd;
    for (i=0; i < N; i++)
    {
        totVelSqd +=
(atom[i].vel.x*atom[i].vel.x)+(atom[i].vel.y*atom[i].vel.y)+(atom[i].ve
l.z*atom[i].vel.z);
    }
    instaT = (2*KE)/(3*N*kb);
    double TF = sqrt(temperature/instaT);
    for (i=0; i < N; i++)
    {
        atom[i].vel.x *= TF;
        atom[i].vel.y *= TF;
        atom[i].vel.z *= TF;
    }
}

void initialEnergy()
{
    int i,j;
    double KE = 0.0;
    double PE = 0.0;
    double TE = KE + PE;
    double vx, vy, vz;
    double dx, dy, dz;
    double r2;
    double s2r2;
    for(i=0; i<N; i++)
    {
        vx = atom[i].vel.x;
        vy = atom[i].vel.y;
        vz = atom[i].vel.z;
        KE += 0.5*(pow(vx,2) + pow(vy,2) + pow(vz,2));
    }
    for(i = 0; i < N-1; i++)
    {
        for(j=i+1; j<N; j++)
        {
            dx = atom[i].pos.xm - atom[j].pos.xm;
            dy = atom[i].pos.ym - atom[j].pos.ym;
            dz = atom[i].pos.zm - atom[j].pos.zm;
            r2 = pow(dx,2) + pow(dy,2) + pow(dz,2);
            s2r2 = pow(sigma,2)/r2;
            PE += 4*epsilon*(pow(s2r2,6) - pow(s2r2,3));
        }
    }
}

```

```

    }
}
T_Thermostat(KE);          //pg 46 CSoL
TE = KE + PE;
}

void verlet()              //pg 79 CSoL, pg 80 for other methods 81s76
{
    int i, j;
    for (i = 0; i < limit; i++)
    {
        initialForce();
        for (j = 0; j < N; j++)
        {
            atom[i].pos.xp = 2 * atom[i].pos.x - atom[i].pos.xm +
(atom[i].force.x) * dt * dt;
            atom[i].pos.yip = 2 * atom[i].pos.y - atom[i].pos.ym +
(atom[i].force.y) * dt * dt;
            atom[i].pos.zp = 2 * atom[i].pos.z - atom[i].pos.zm +
(atom[i].force.z) * dt * dt;

            atom[i].vel.x = 0.44915 * (atom[i].pos.xp - atom[i].pos.xm)
/ dt;
            atom[i].vel.y = 0.5 * (atom[i].pos.yip - atom[i].pos.ym) /
dt;
            atom[i].vel.z = 0.5 * (atom[i].pos.zp - atom[i].pos.zm) /
dt;

            atom[i].pos.xm = atom[i].pos.x;
            atom[i].pos.ym = atom[i].pos.y;
            atom[i].pos.zm = atom[i].pos.z;

            atom[i].pos.x = atom[i].pos.xp;
            atom[i].pos.y = atom[i].pos.yip;
            atom[i].pos.z = atom[i].pos.zp;

        }
        initialEnergy();
    }
}

int main()
{
    initialPosition();
    initialForce();
    verlet();
    //printResults();
    return 0;
}

```

6.2 Appendix B – Water box calculations

Table 4. Water box calculations to develop system of typical water density

Desired radius (Å)	Volume (Å ³)	Mass (g)	Moles of water (mol)	N	Side Length (Å)
44.9	379164.47	3.79E-19	2.10E-20	12629	72.37844
49.9	520463.46	5.20E-19	2.89E-20	17335.3	80.4384
59.9	900262.33	9.00E-19	5.00E-20	29985.43	96.55832
69.9	1430606.3	1.43E-18	7.94E-20	47649.83	112.6782

6.3 Appendix C – Radial Distribution Function Script

```
/*David Laur*/
/*Basic script to generate RDF between protein COM and water*/

proc rdf {rdf_out} {
  for {set n 4} {$n < 24795} {incr n 3} { //Loop all water
    set sel1 [atomselect top "protein"]
    set sel2 [atomselect top "index $n"]
    set nf [molinfo top get numframes]
    set outfile [open $rdf_out a]
    for {set i 0} {$i < $nf} {incr i} { //Loop all frames
      if {$n == 24794 && $i == 0} {
        break
      }
      else {

        puts "frame $i of $nf"
        $sel1 frame $i
        $sel2 frame $i
        set com1 [measure center $sel1 weight mass]
        set com2 [measure center $sel2 weight mass]
        set simdata($i.r)[veclength [vecsub $com1$com2]]
        puts $outfile "$i , $simdata($i.r)"

      }
    }
  }
  close $outfile
}
}
```

6.4 Appendix D – Hydrogen bond data

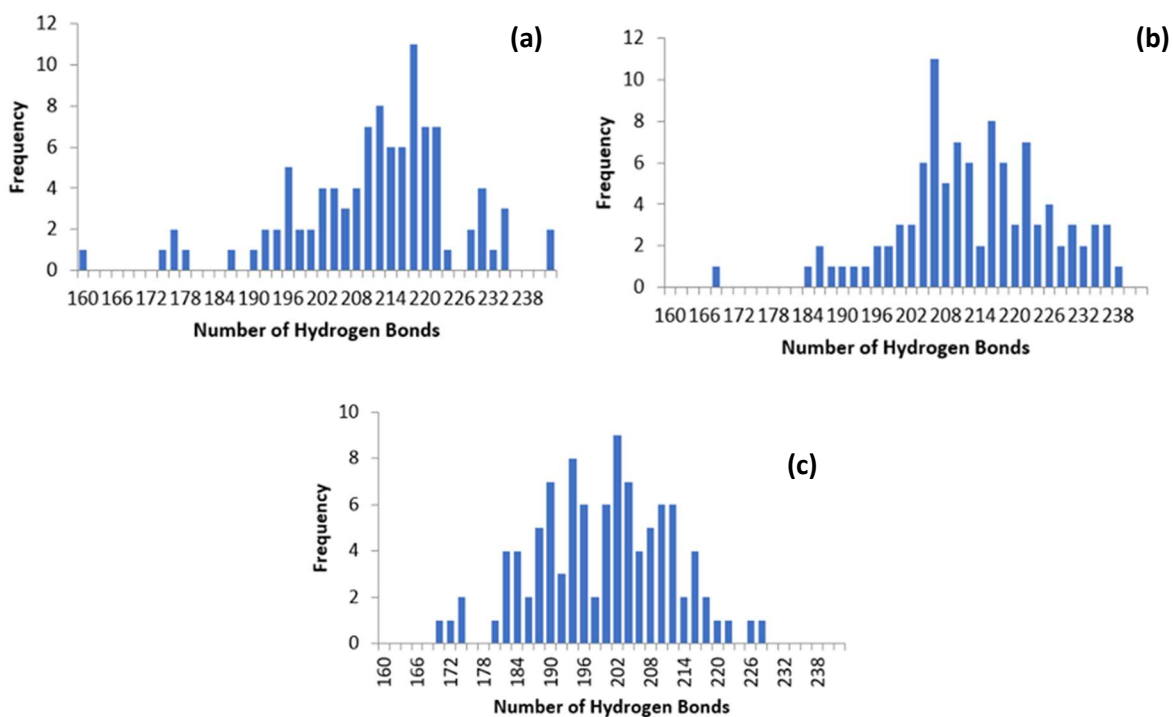


Figure 9. Histogram depicting hydrogen bond frequency within spherical confinement radii of 45 Å. (a) - 0Å, (b) - 10Å, (c) - 20 Å separation

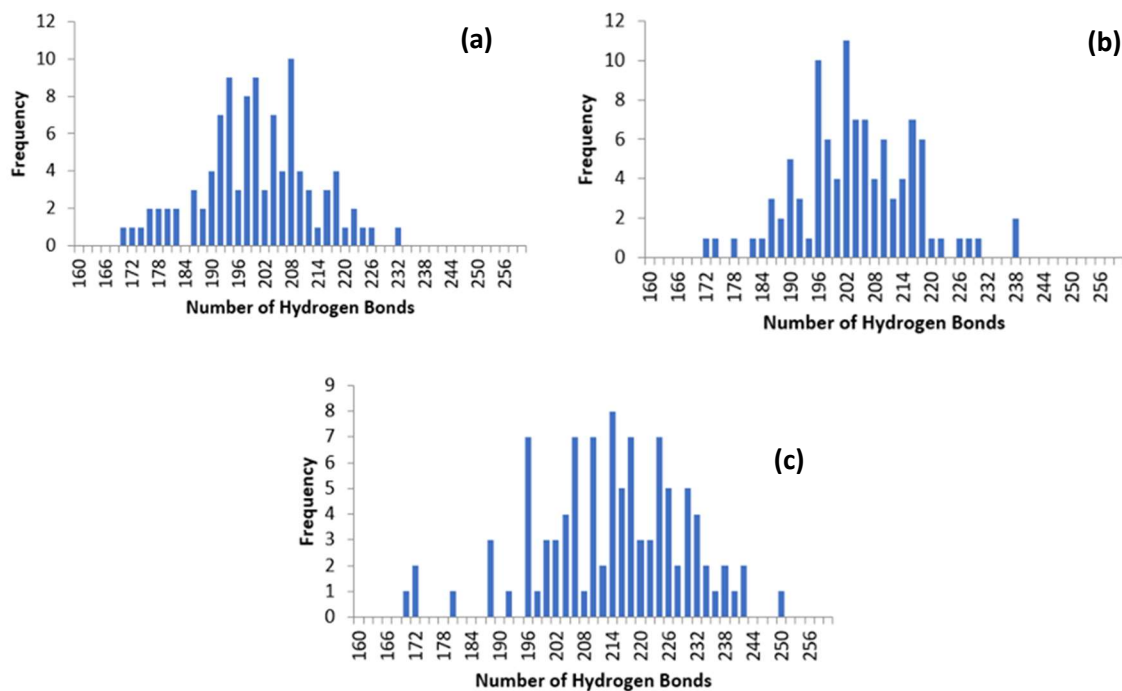


Figure 10. Histogram depicting hydrogen bond frequency within spherical confinement radii of 60 Å. (a) - 0Å, (b) - 10Å, (c) - 20 Å separation

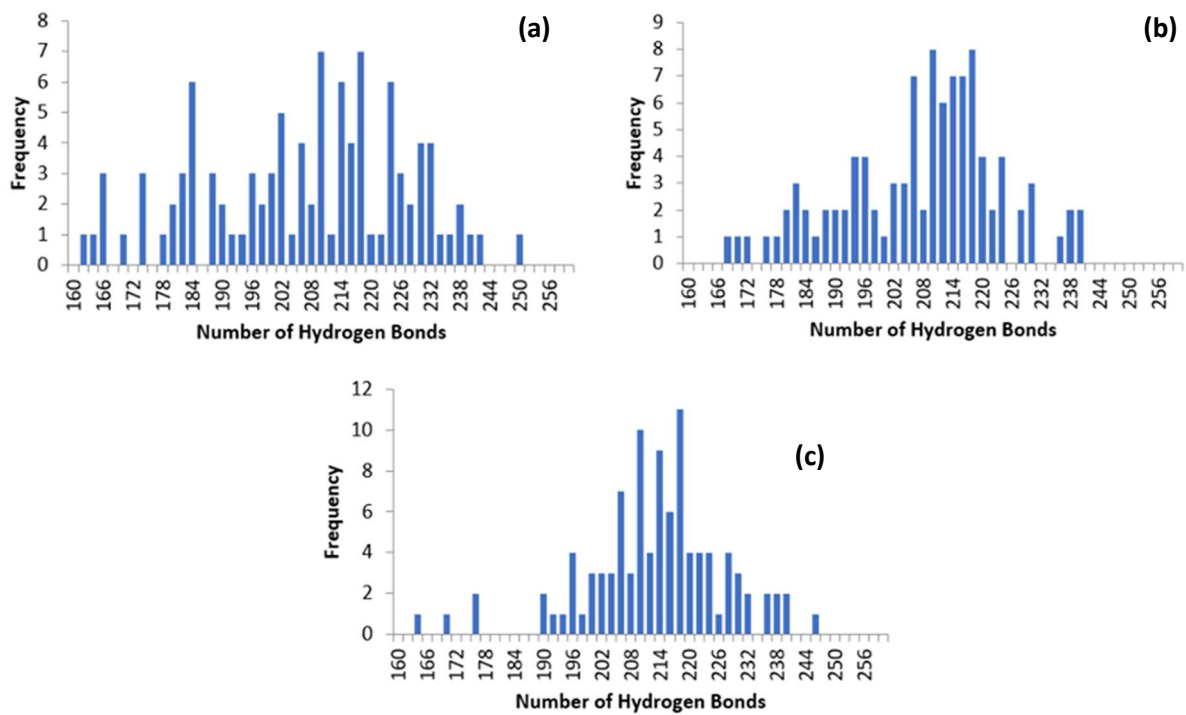


Figure 11. Histogram depicting hydrogen bond frequency within spherical confinement radii of 70 Å. (a) - 0Å, (b) - 10Å, (c) - 20 Å separation

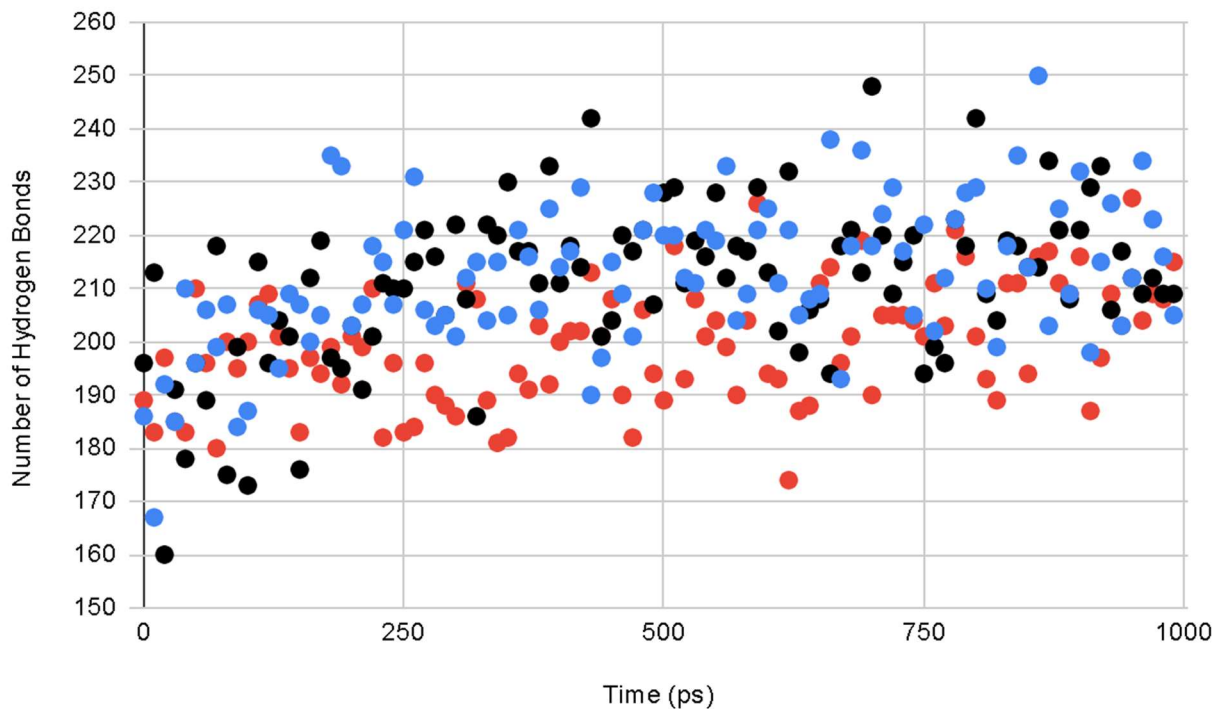


Figure 12a. Hydrogen bond frequency versus simulation progression within spherical confinement radii of 45 Å. Red - 0Å, Black - 10Å, Blue - 20 Å.

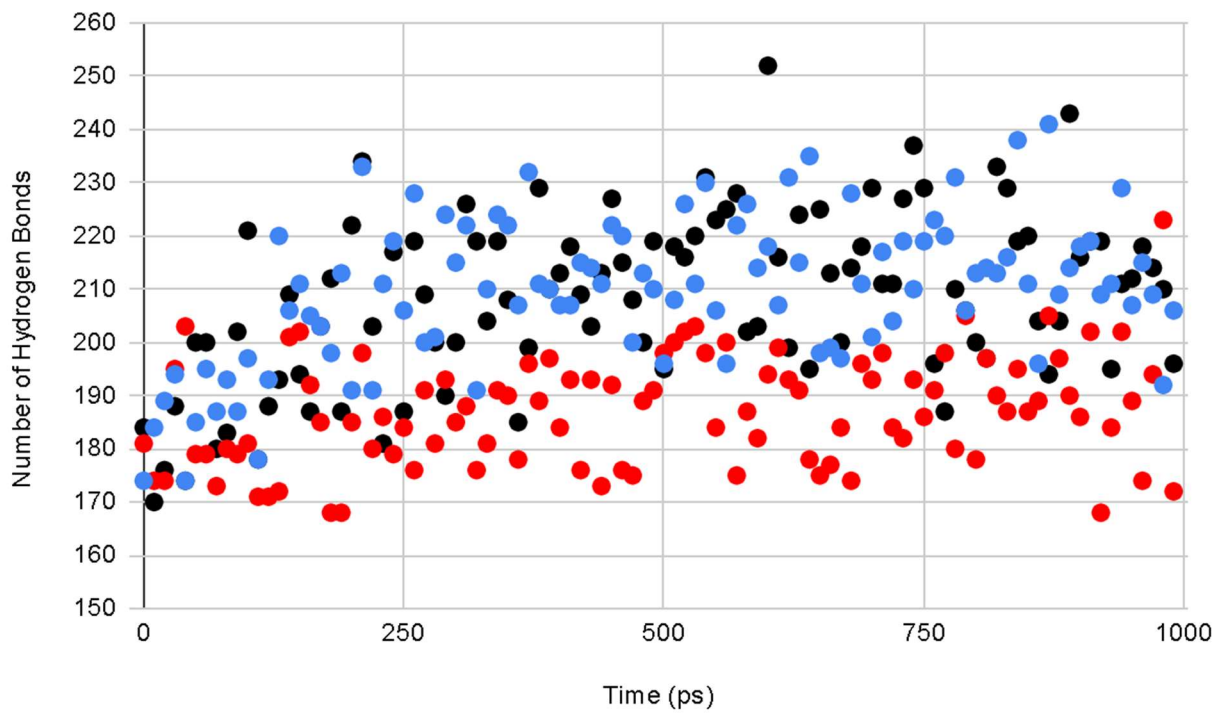


Figure 12b. Hydrogen bond frequency versus simulation progression within spherical confinement radii of 50 Å. Red - 0Å, Black - 10Å, Blue - 20 Å.

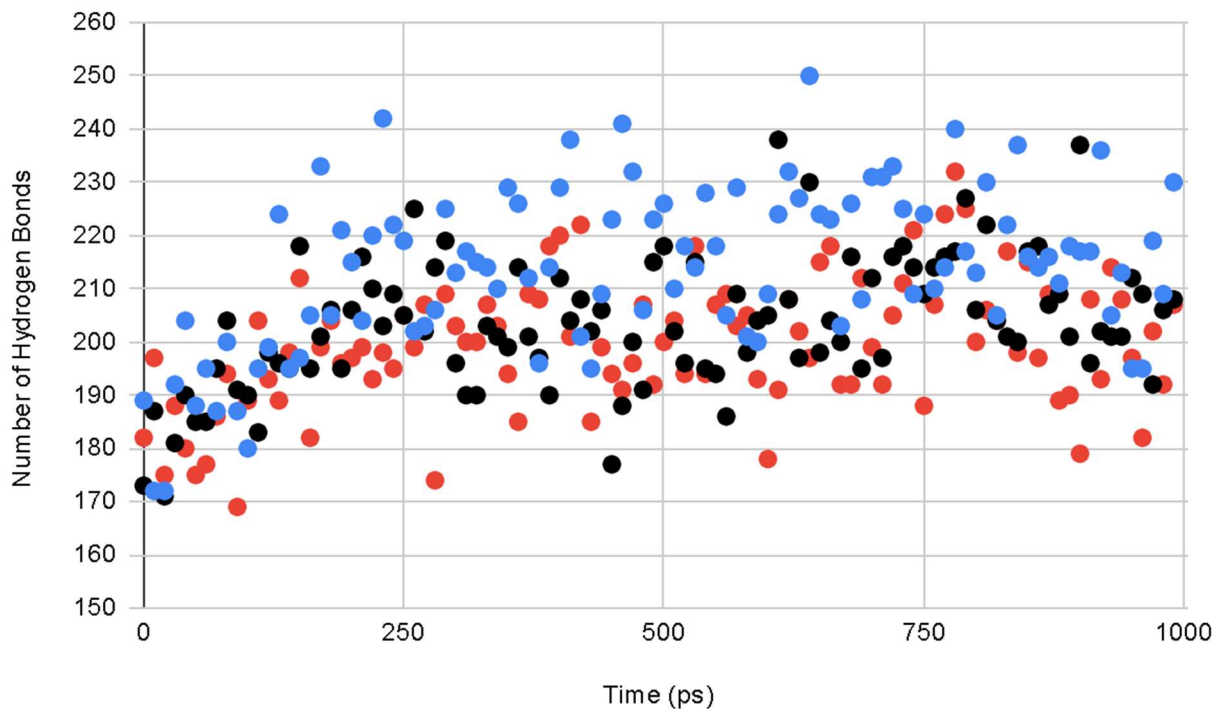


Figure 12c. Hydrogen bond frequency versus simulation progression within spherical confinement radii of 60 Å. Red - 0Å, Black - 10Å, Blue - 20 Å.

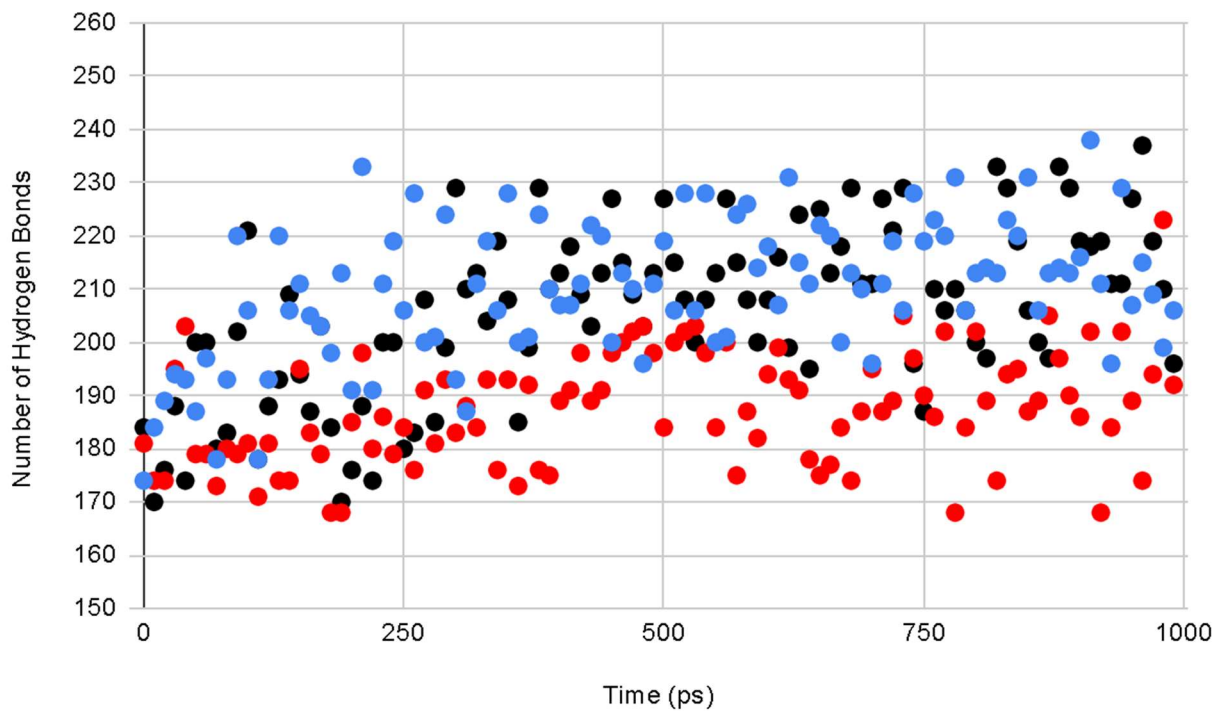


Figure 12d. Hydrogen bond frequency versus simulation progression within spherical confinement radii of 70 Å. Red - 0 Å, Black - 10 Å, Blue - 20 Å.

6.5 Appendix E – Potential Energy Fluctuation Plot

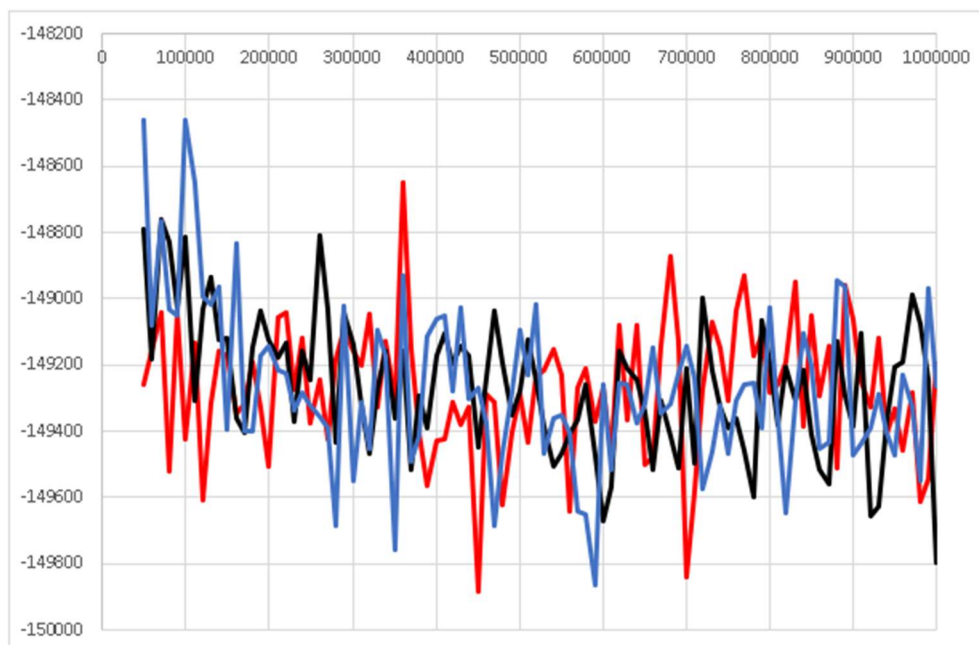


Figure 13a. Potential energy fluctuation versus time step within a spherical confinement radius of 45 Å. Red - 0 Å, Black - 10 Å, Blue - 20 Å.

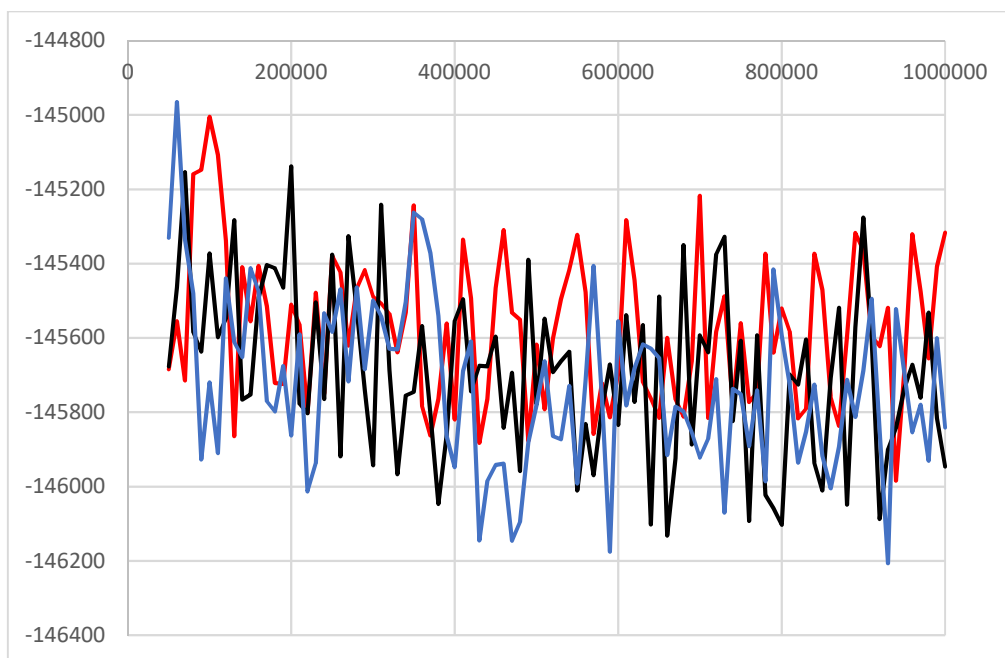


Figure 13b. Potential energy fluctuation versus time step within a spherical confinement radius of 50 Å. Red - 0Å, Black - 10Å, Blue - 20 Å.

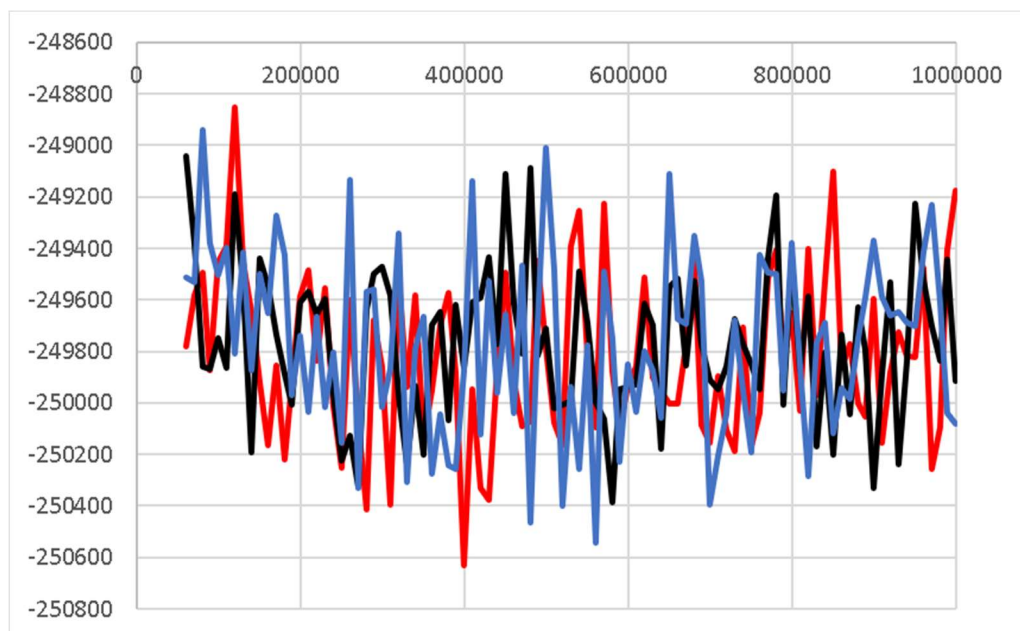


Figure 13c. Potential energy fluctuation versus time step within a spherical confinement radius of 60 Å. Red - 0Å, Black - 10Å, Blue - 20 Å.

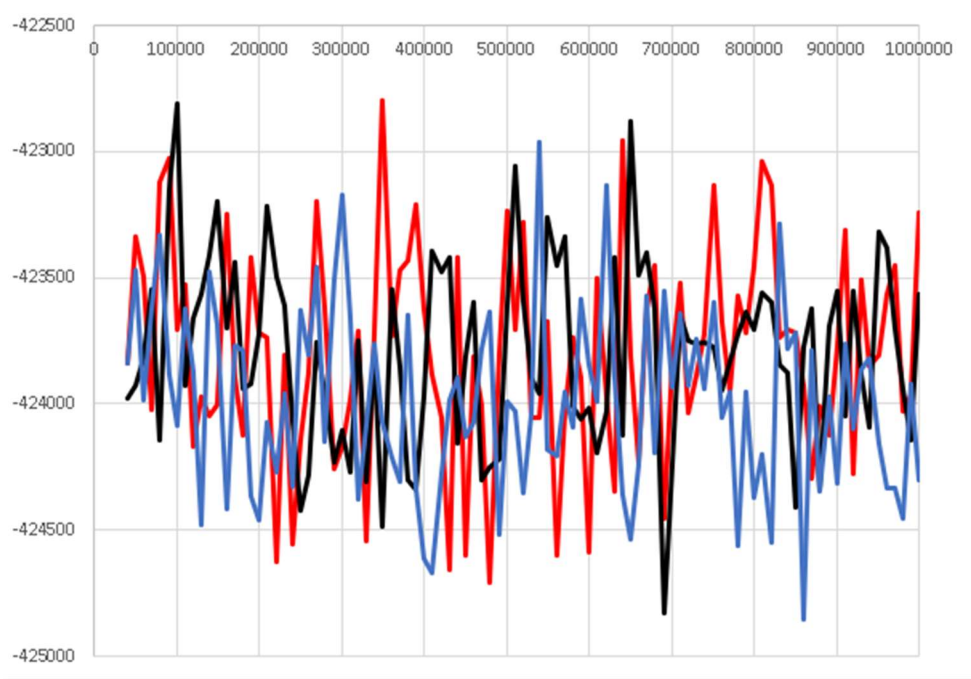


Figure 13d. Potential energy fluctuation versus time step within a spherical confinement radius of 70 Å. Red - 0 Å, Black - 10 Å, Blue - 20 Å.